Ion-Catalyzed Synthesis of Microporous Hard Carbon Embedded with Expanded Nanographite for Enhanced Lithium/Sodium Storage

Zhi-Long Yu,[†,#] Sen Xin,[‡,§,#] Ya You,[§] Le Yu,[⊥] Yue Lin,[†] Da-Wei Xu,[‡] Chan Qiao,[†] Zhi-Hong Huang,[†] Ning Yang,[†] Shu-Hong Yu,*[,†] and John B. Goodenough*[,§]

[†]Division of Nanomaterials & Chemistry, Hefei National Laboratory for Physical Sciences at the Microscale, Collaborative Innovation Center of Suzhou Nano Science and Technology, Department of Chemistry, CAS Center for Excellence in Nanoscience, Hefei Science Center of CAS, University of Science and Technology of China, Hefei 230026, P. R. China

[‡]School of Chemistry and Chemical Engineering, Hefei University of Technology, Hefei 230009, P. R. China

[§]Department of Mechanical Engineering, The University of Texas at Austin, Austin, Texas 78712, United States

[⊥]Key Laboratory of Synthetic and Natural Functional Molecule Chemistry of Ministry of Education, College of Chemistry & Materials Science, Shaanxi Key Laboratory of Physico-Inorganic Chemistry, Northwest University, Xi'an 710127, P. R. China

Ⓢ Supporting Information

ABSTRACT: Hard carbons attract myriad interest as anode materials for high-energy rechargeable batteries due to their low costs and high theoretical capacities; practically, they deliver unsatisfactory performance due to their intrinsically disordered microarchitecture. Here we report a facile ion-catalyzed synthesis of a phenol−formaldehyde resin-based hard-carbon aerogel that takes advantage of the chelation effect of phenol and Fe^{3+}, which consists of a three-dimensionally interconnected carbon network embedded with hydrogen-rich, ordered microstructures of expanded nanographites and carbon micropores. The chelation effect ensures the homodispersion of Fe in the polymer segments of the precursor, so that an effective catalytic conversion from sp^3 to sp^2 carbon occurs, enabling free rearrangement of graphene sheets into expanded nanographite and carbon micropores. The structural merits of the carbon offer chances to achieve lithium/sodium storage performance far beyond that possible with the conventional carbon anode materials, including graphite and mesocarbon microbeads, along with fast kinetics and long cycle life. In this way, our hard carbon proves its feasibility to serve as an advanced anode material for high-energy rechargeable Li/Na batteries.
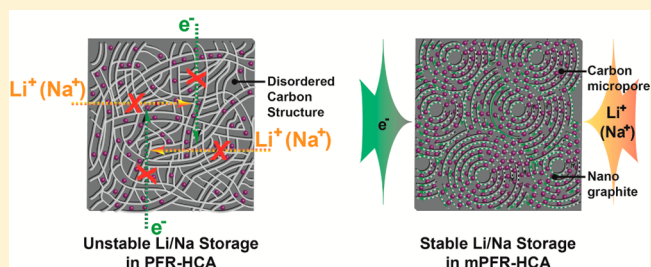
INTRODUCTION

Graphitic carbon, now commonly used as the anode of lithium-ion batteries powering hand-held devices, cannot be used safely in a large-scale battery for powering an electric road vehicle or for stationary storage of electric power for the grid—it has too low an energy density and too low a charging rate (that is, without plating of metallic lithium).[1−23] High-capacity elemental cathodes such as sulfur and oxygen require to pair with a carbon anode with low voltage, light weight, low cost, and a much higher capacity and safe rate of charge.[24−28] One proposed solution is a hard-carbon anode commonly prepared by pyrolysis of phenolic polymers such as phenol−formaldehyde resin (PFR).[29−32] As described by the "house of cards" model, hard carbon (HC) consists mainly of single graphene layers randomly packed in a disordered arrangement.[33,34] This structure provides nanosized pores for the insertion of Li^+ or Na^+ ions along with the large surface area of graphene sheets for adsorption of the guest Li^+ or Na^+, thus offering a large capacity.[35−38] However, recent works mostly boast the capacity advantage of HC while neglecting its defects of low conductivity and poor electrochemical stability due to its

disordered microarchitecture. This hard-carbon anode has two fatal flaws: poor electronic conductivity and poor electrochemical cycling stability. Previous attempts to improve the HCs' electrochemical performance have been focused on either creating a more ordered graphene morphology[30,39,40] or introducing a graphitic component,[41,42] but the product still retained its insintrically disordered microarchitecture.

In this work, we present a fundamental solution to improve the poor electrochemistry of PFR-derived hard-carbon aerogel (PFR-HCA), that is, chemical introduction of two carbon components (ordered expanded nanographites and carbon micropores) to yield a modified carbon (mPFR-HCA) with improved alignment of carbon interlayers and increased hydrogen content. In the electrochemical reaction with alkali metals (i.e., Li and Na), both components of the mPFR-HCA enable stable storage through both interlayer intercalation (expanded nanographites) and interfacial adsorption (micropores), while the increased H content provides more storage

sites. The mPFR-HCA serves as a mixed guest ion/electronic conductor with an accelerated electrochemical reaction, a higher capacity, and an improved cycling stability for the storage of Li^+ or Na^+ in high-energy rechargeable Li/Na batteries.

■ RESULTS AND DISCUSSION

Material Synthesis and Characterization. Pristine PFR-HCA was synthesized by annealing a modified chitosan-templated PFR gel (inset in Figure S1a, in the Supporting Information), as reported elsewhere;[43] its properties were compared to those of the modified mPFR-HCA. According to Figure S1, both the PFR gel before annealing and the annealed PFR-HCA show a compact net-like structure with beads of ∼30 nm in diameter (inset of Figure S1b). A high-resolution transmission electron microscopy (HRTEM) image further reveals a disordered nanostructure (Figure S2a). Metal ions such as Fe^{3+} are frequently used as catalysts to modify the microstructures of HCs. However, simply mixing the metal catalysts with phenolic solids or oligomers such as resol and novolac makes it difficult to distribute uniformly the metal into the preformed polymer at the nanoscale. The chelation effect of metal ions with polymer monomers can improve the dispersion of metal catalysts into carbon precursor units, yielding a better catalytic effect. Based on this concept, a facile metal-ion (Fe^{3+}) catalytic graphitization process[44−47] was adopted to generate ordered carbon components (expanded nanographite) and micropores and yield mPFR-HCA (Figure 1). During the
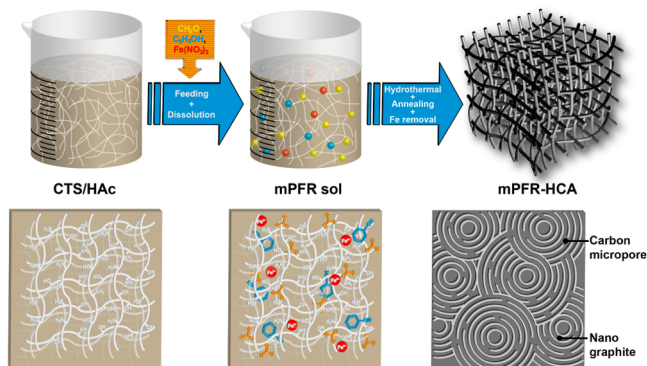

Figure 1. Schematic illustration showing the typical synthesis of the mPFR-derived hard-carbon aerogel.

catalysis, the gel macrostructure and the coral-like micro-structure consisting of nanofibers of ∼25 nm in diameter remain (Figure S3a−c), and the Fe^{3+} ions are distributed homogeneously in the nitrogen-/oxygen-containing carbon precursor, as confirmed by the elemental mappings obtained by energy-filtered transmission electron microscopy (EFTEM, see Figure S3d−g). After annealing, Fe species, including Fe and Fe_2O_3, are observed by X-ray diffraction (XRD, Figure S4a) and TEM (Figure S5a). However, the signal of Fe_3C is obscured (Figure S4a) due to irreversible decomposition of Fe_3C into Fe and C, which means a low content and poor crystallinity of Fe_3C. To confirm the existence of Fe_3C and better reveal the Fe phases in the mPFR-HCA(Fe) hybrid, we separately increased the Fe^{3+} amount to 4 (2 mmol g^{-1}, denoted as mPFR-HCA(Fe 4×)) and 12 (6 mmol g^{-1}, denoted as mPFR-HCA(Fe 12×)) times the original amount (0.5 mmol g^{-1}). The XRD peaks of Fe_3C are clearly seen in the two

hybrids (Figure S4b), confirming that the small amount of Fe^{3+} is responsible for the difficult detection of the Fe_3C phase. Due to the migration and accumulation of Fe species in the carbon, Fe nanoparticles finally form and are embedded in the expanded nanographite, generating an ordered, onion-like structure (Figure S5a). After complete removal of Fe species by nitric acid (as confirmed by comparison between the XRD patterns in Figure 3a and Figure S4a, and the EDX spectra in
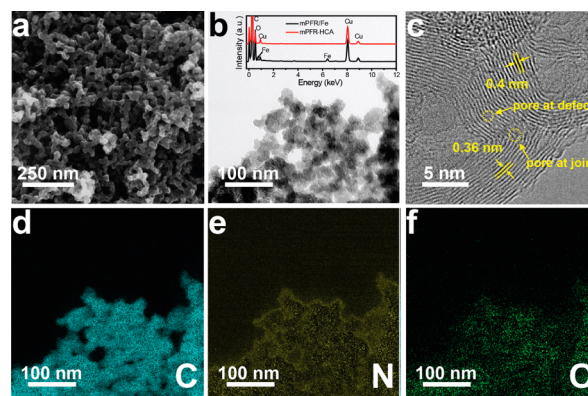

Figure 2. Morphological and elemental characterizations of the mPFR-HCA: (a) scanning electron microscopy (SEM) image and (b) transmission electron microscopy (TEM) image of the mPFR-HCA (inset shows the EDX spectra collected before and after Fe removal), (c) HRTEM image taken from a carbon nanofiber, and corresponding EFTEM elemental mappings of (d) C, (e) N, and (f) O.

the inset of Figure 2b), the obtained mPFR-HCA still shows an aerogel appearance (Figure S6) with coral-like morphology (Figure 2a,b). From the HRTEM image, the mPFR-HCA contains ordered nanographite domains with an average d-spacing of 0.36−0.4 nm (Figure 2c). C micropores with a size of ∼0.8 nm are also found in the mPFR-HCA (Figure 2c and Figure S5b). The TEM image agrees well with the XRD patterns (Figure 3a), in which the mPFR-HCA shows a sharp peak at $2\theta = 25.6°$, slightly smaller than the (002) peak of graphite ($2\theta = 26.54°$), which gives a d-spacing of 3.356 Å and indicates an expanded interlayer according to the Bragg equation.[21] The Raman spectra also show an increase from 0.96 to 1.06 in the I_g/I_d value after chemical modification (Figure 3b), confirming an elevated degree of graphitization of carbon. C1s X-ray photoelectron spectra (XPS) were also collected for both modified and unmodified carbons (Figure 3c), in which four peaks denoting sp^2 C, sp^3 C, C—O, and O—C=O were deconvoluted with increasing binding energies,[48] and the result was consistent with the overlapped EFTEM mapping signals of C and O in the mPFR-HCA (Figure 2d,f). The EFTEM also showed a uniform distribution of nitrogen (Figure 2d,e), which has been shown to be beneficial to enhance the electronic conductivity of carbon.[49] The sp^2 C content increases from 69.6 to 73.3 at.%, while the sp^3 C content decreases from 30.4 to 26.7 at.% after modification (Figure 3c), which is consistent with the Raman and XRD results, showing a much improved alignment of the graphene sheets.[50]

The porous structures of the two carbons were also investigated. According to the nitrogen adsorption−desorption isotherms collected on both carbons (Figure 3d and Figure S7a), the mPFR-HCA shows a significant type I adsorption, which implies a rich existence of micropores.[31,51] The pore-size
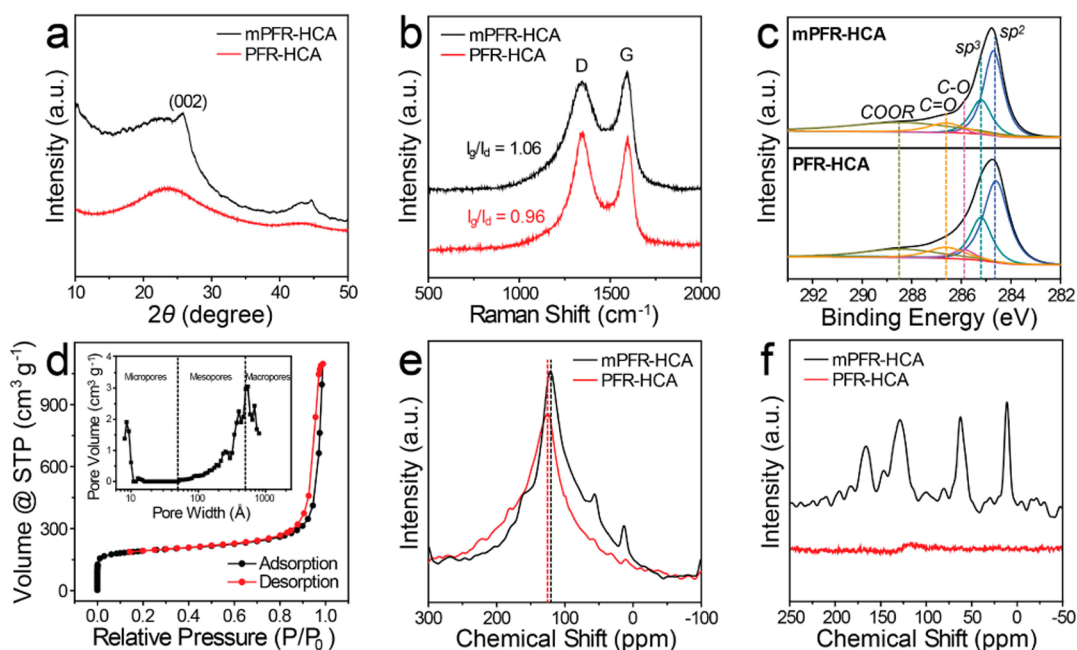
Figure 3. Structural characterization results: (a) XRD patterns, (b) Raman spectra, and (c) XPS C1s spectra of the mPFR-HCA and PFR-HCA; (d) N_2 adsorption−desorption isotherms of the mPFR-HCA (inset shows the corresponding DFT pore size distribution); and (e) ^{13}C DP/MAS and (f) ^{13}C CP/MAS NMR spectra of the mPFR-HCA and PFR-HCA.
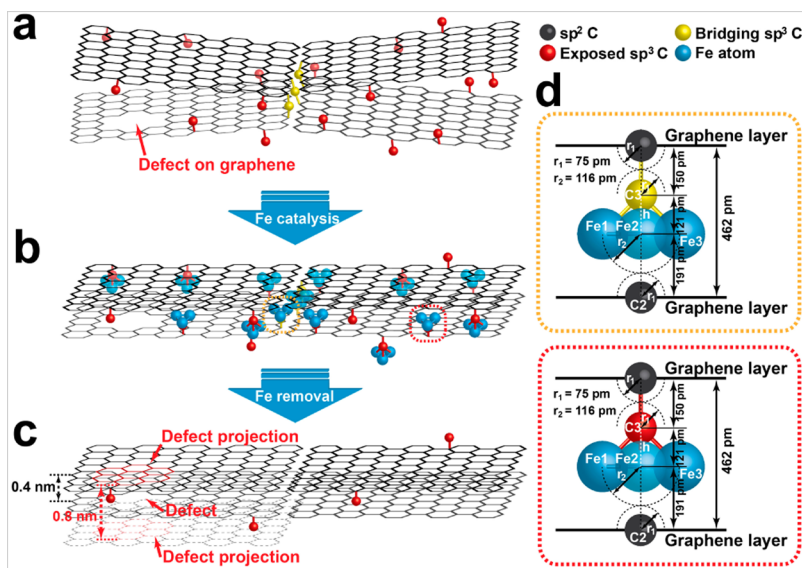

Figure 4. Simulations showing the Fe_3C modification to generate locally graphitized carbon: (a) densely packed carbon monolayers bridged by sp^3 C before modification (rich in sp^3 carbon at edges and in bridges); (b) graphene monolayers with Fe_3C clusters formed in between; (c) formation of locally graphitized carbon (containing less sp^3 carbon) after Fe removal and formation of micropores at defects in the graphene sheets. (d) Schematic illustration showing a single Fe_3C cluster formed on an sp^3 carbon between two carbon monolayers. In calculating the d-spacing, the covalent radii of Fe (116 pm) and C (75 pm) and the height of optimized pyramid Fe_3C isomer (121 pm) are employed.

distribution calculated by using the non-local density functional theory (DFT) demonstrates a concentrated micropore size of ~0.8 nm (inset of Figure 3d), and the cumulative pore distribution (Figure S8) further indicates that ~90% of the micropore volume is contributed by micropores of 0.7−0.9 nm in diameter. In contrast, the PFR-HCA shows a negligible micropore contribution (Figure S7b). The chemical modification also helps to enlarge the Brunauer−Emmett−Teller specific surface area of the mPFR-HCA to 664 m^2 g^{-1}, which is nearly double that of the PFR-HCA (380 m^2 g^{-1}).

Nuclear magnetic resonance (NMR) spectra were also collected from the two carbons to investigate their carbon constituents. As can be seen from Figure 3e, the ^{13}C direct polarization/magic angle spinning (DP/MAS) spectra show a strong, broad line in the aromatic region and other weak peaks indicative of aliphatic carbons (characteristic peaks include the carboxyl carbon peak at ~160 ppm and the methoxyl group peak at ~60 ppm).[52,53] The very intense band at ~125 ppm is assigned to the sp^2 carbon of the turbostratic disordered graphene sheets.[52] The mPFR-HCA shows a broader sp^2 carbon peak and a smaller average chemical shift than the

PFR-HCA, owing to its higher electric conductivity and the graphitized regions (Figure 3e).[54] The peak at ~20 ppm is attributed to sp^3 carbon because of its small chemical shift anisotropy (narrow line width); an sp^3 carbon should have a high symmetry of its atomic neighbors.[55] As a HC, the PFR-HCA shows no sp^3 carbon peak, due to the uncertain chemical environment of a carbon that connects with an uncertain amount of H or sp^2 C or sp^3 C or other oxide groups (Figure 3e).[55] The sp^3 C peak in mPFR-HCA, compared to that in PFR-HCA, is consistent with a better alignment of the graphene sheets, giving a more uniform environment of the connecting sp^3 C. Figure 3f shows four distinct peaks in the ^{13}C cross-polarization/magic angle spinning (CP/MAS) spectrum of mPFR-HCA, but no resonance peaks in PFR-HCA,[54] because most carbon atoms of the well-carbonized PFR-HCA are distant from protons in the interior of the aromatic planes. Only a small portion of the C nuclei will be effectively cross-polarized.[54] Thus, PFR-HCA shows a poor resolution of signals due to the low H content (Figure 3f), exhibiting no sp^3 peak and even no sp^2 peak.[54] Due to the Fe^{3+} catalytic effect, sp^3 C bridges are broken, and the exposed sp^3 C can connect with more H atoms. Thus, sp^3 C and sp^2 C can both exhibit obvious peaks in the CP/NMR spectrum (Figure 3f). This result is consistent with our elemental analysis results on the two carbons (Table S1), which reveal a higher H content of the mPFR-HC (2.45 wt%) than the unmodified PFR-HCA (2.09 wt%). The conclusion is even important for application in lithium-ion batteries: as hydrogen exchange is also a Li storage route in HCs,[34] the hydrogen content in the HC inevitably affects the Li storage capacity. Besides, the better alignment of the graphene sheets allows faster electronic transfer between the sheets as well as better alignment of the interstitial space for ionic transport.

Formation Mechanism of Expanded Nanographite and Carbon Micropores. To figure out the origins of the above structural differences between the mPFR-HCA and the PFR-HCA, the mechanism of the chemical modification process of HC was studied. According to the "house of cards" model, the randomly packed graphene sheets in PFR-HCA consist of sp^2 carbons in condensed aromatic structures and sp^3 carbons at the edge. Some of these sp^3 carbons connect with H, while others act as bridges to link adjacent graphene layers (Figure 4a and Figure S9a). Since the sp^3 carbon is originated from methylene of PFR, that is, outside the benzene ring plane,[56] it is difficult to graphitize HCs at high temperatures. During the chemical modification of PFR-HCA, a strong chelation effect of phenol helps to trap Fe^{3+} in the PFR polymer segments, where the Fe^{3+} is more likely to meet and react with the sp^3 carbons. The reaction breaks the chemical bonding among graphene sheets to generate a single four-atom iron carbide (Fe_3C), which then migrates, accumulates, and decomposes into sp^2 carbons.[46] In this way, the disordered graphene sheets may be rearranged. Based on our geometric optimizations performed on a single Fe_3C cluster, three isomers were determined separately, one with a pyramid configuration and two planar configurations (Figure S10). Among the three isomers, the pyramid isomer (Isomer I) possessed the lowest energy and a dense structure and was thereby selected as the optimized configuration to perform the mechanism study. Based on this configuration, simulations were further employed on the chemical modification process of the mPFR-HCA (Figure 4 and Figure S9). Given the "house of cards" model,[33,34,57] the sp^3 C bridge adjacent graphene sheets

composed of one (in the case of densely packed graphene layers, see Figure 4a) or more sp^3 C atoms (in the case of loosely packed graphene layers, see Figure S9a). If H-bonded sp^3 C atoms or single bridging atoms are sandwiched between two close-packed, adjacent graphene layers (Figure 4a), single Fe_3C clusters will form, migrate, and accumulate during the catalysis process to yield ordered nanographite domains with slightly expanded d-spacing of 0.36−0.4 nm (Figure 2c) since the dimensions of Fe_3C (~0.45 nm) are larger than the (002) d-spacing of graphite (~0.34 nm) (Figure 4b−d). At a defect in a graphene layer, the d-spacing will be doubled; hence, a C micropore of ~0.8 nm may form (Figure 4a−c). If two or more bridging C atoms are sandwiched in loosely packed graphene sheets (Figure S9a), two Fe_3C clusters (in a bottom-to-bottom fashion) or patches may form to further expand the carbon interlayer spacing into an arch domain of ~0.8 nm (Figure S9b−d), which contributes to another possible source of the C micropore (Figure S9c). Since the practical existences of both types of micropores have been confirmed by the HRTEM images (Figure 2c and Figure S5b), it is highly possible that the ~0.8 nm carbon micropores are generated during the modification process. Hence, it is clear that the chemical modification by Fe^{3+} helps to generate expanded nanographite and C micropores. It is also noted that, due to the randomly arranged graphene sheets in the PFR-derived HC, it is impractical to convert all sp^3 C into sp^2 C (Figure 4c and Figure S9c), as confirmed by the XPS result (Figure 3c). However, the trace existence of sp^3 C at the edges of the graphene layers may help in bridging the adjacent graphene layers, which is beneficial to improving the structural stability of the HC.

Electrochemical Properties of Li-Ion Battery. In previous works, the poor Li storage performance of HC was ascribed to its poor alignment of graphene sheets, which impedes the migration of Li^+ and e^-. Herein, by introducing locally graphitized nanostructures and ordered carbon micropores into HC, we can expect improved performance. Based on this concept, the as-prepared mPFR-HCA was incorporated into working electrodes, which were then paired with Li to assemble prototype Li half-cells for electrochemical tests. The unmodified PFR-HCA was also tested for comparison. Figure S11 compares the cyclic voltammograms (CVs) of the two carbons with Li^+/Na^+ intercalation. For Li^+ intercalation in mPFR-HCA (Figure S11a), the CV shows five well-defined peaks: those at 1.82, 1.55, and 1.16 V versus Li^+/Li (the same below) are irreversible, while those at 0.20 and <0.05 V are reversible. The largest irreversible peak, at 1.16 V, corresponds to the formation of a solid electrolyte interface (SEI),[58] and the two other peaks correspond to the reduction of oxygen of the C—O and C═O bonds.[48] The peak at 0.20 V suggests a significant interfacial Li storage in those carbon micropores and expanded nanographites.[57] The last peak, at <0.05 V, demonstrates the Li insertion into nanographite and is largely overlapped with the broad interfacial storage peak at 0.2 V. Corresponding to the last two reduction peaks, two oxidation peaks are found at 0.53 and 0.65 V in the reverse anodic process, implying a partially reversible Li de-intercalation from the carbon. The two pairs of redox peaks gradually stabilize and become highly reversible in the subsequent CV scans, implying a steady Li uptake/release of the mPFR-HCA.

The Li^+ reaction CV of PFR-HCA (Figure S11c) is completely different from that of mPFR-HCA; the peak of the cathodic scan of Figure S11a is either missing or greatly
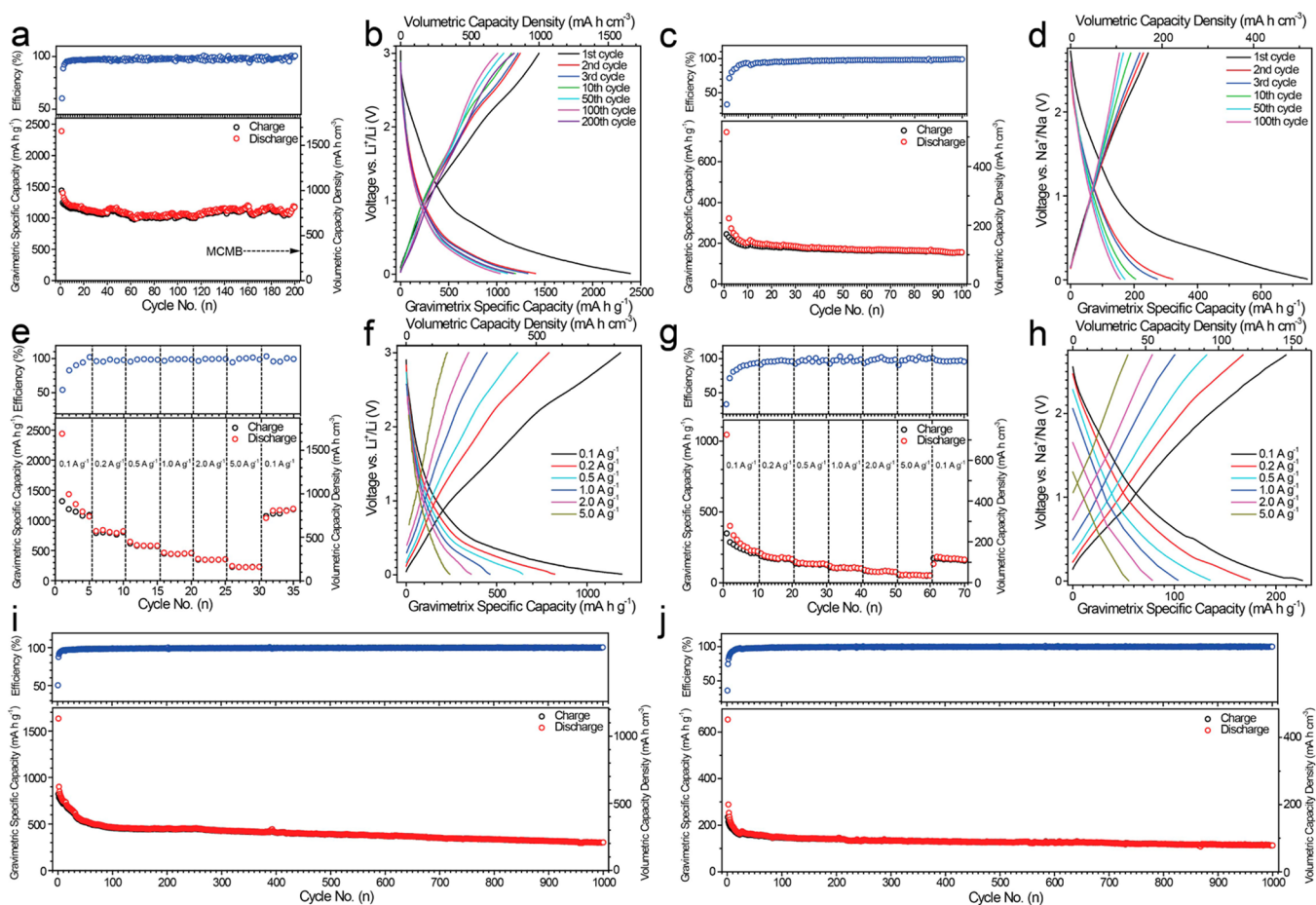
Figure 5. Electrochemical performances of the mPFR-HCA: cycling performance and GDC profiles of the mPFR-HCA at 0.1 A g^{-1} in Li half-cells (a,b) and Na half-cells (c,d); cycling performance and GDC profiles of the mPFR-HCA at various current densities gradually increasing from 0.1 to 5.0 A g^{-1} and then back to 0.1 A g^{-1} in Li half-cells (e,f) and Na half-cells (g,h); and long-term cycling performance of the mPFR-HCA at a high current density of 1 A g^{-1} in Li half-cells (i) and Na half-cells (j). The gravimetric specific capacities were calculated on the basis of the mass of the mPFR-HCA on the electrode, and the volumetric capacity densites were calculated on the basis of the tap density of the mPFR-HCA: 0.6937 g cm^{-3}.

reduced, which is consistent with the lack of Li$^+$ access not only to the oxygen atoms (although Table S1 demonstrates a higher oxygen content of PFR-HCA than that of mPFR-HCA) but also into the HCA electrode. Moreover, the peak at 0.20 V in Figure S11a appears to have completely vanished, while the peak at <0.05 V is largely weakened, as expected when there are negligible ordered nanocarbon regions. In the subsequent scans, the reduction peaks continue to decay, which further supports the electrochemical instability of PFR-HCA. A galvanostatic intermittent titration technique (GITT) was employed to perform kinetic analysis on the Li intercalations of both anodes. An extremely low current density of 50 mA g^{-1} with a long relaxation period of 10 h was applied upon discharging to ensure the electrochemical reactions of "quasi-static" processes. According to the measurement, the evolution of the quasi-equilibrium potentials decreases continuously with x calculated as Li$_x$C in both anodes, indicating that the Li intercalations in both carbons are single-phase rather than two-phase reactions as reported in graphite (Figure S12a). The apparent chemical diffusion coefficients (D_{app}) of Li$^+$ as a function of x were also calculated for both anodes according to the GITT results (Figure S12b). Although a similar trend is observed for both carbon anodes, the calculated D_{app} of the mPFR-HCA anode is significantly higher than that of the unmodified PFR-HCA. From Ohm's law, the electronic

conductivity of the mPFR-HCA was measured and compared with that of the unmodified PFR-HCA. The conductivity of mPFR-HCA (1.0 S m^{-1}) is about 2 orders of magnitude higher than that of the PFR-HCA (9.0 × 10^{-3} S m^{-1}). All these results confirm the significant kinetic advantage of mPFR-HCA over the unmodified PFR-HCA.

Cycled at a current density of 0.1 A g^{-1}, the mPFR-HCA shows a steep voltage drop from open-circuit with Li$^+$ insertion, with a small plateau at ~0.80 V in the first cycle, corresponding to the SEI formation and loss of capacity (Figure 5b). A long and flattened slope is observed below 0.5 V (Figure 5b), and the electrochemistry is consistent with an interfacial Li intercalation into carbon micropores and a further insertion into expanded graphite interlayers. In the subsequent cycles, the galvanostatic discharge–charge (GDC) profiles become highly consistent, with major capacity contributions falling into the low-voltage region (Figure 5b), which is beneficial to improving the energy density of a battery. The mPFR-HCA shows an unprecedentedly high gravimetric specific capacity of 2391 mA·h g^{-1} (or a volumetric capacity density of 1659 mA·h cm^{-3}) upon discharge, and then a reversible capacity of 1440 mA·h g^{-1} (or 999 mA·h cm^{-3}) in the first cycle, bringing a reasonable initial Coulombic efficiency (ICE) of 60.2% (Figure 5a,b). From the second cycle, the mPFR-HCA shows a favorable cycling stability, with a capacity steadily maintained between

1100 and 1200 mA·h g^{-1}; in this way, a high reversible capacity of 1180 mA·h g^{-1} (819 mA·h cm^{-3}) is preserved after 200 cycles, which means a tiny average capacity loss of 1.3 mA·h g^{-1} (or 0.9 mA·h cm^{-3}) per cycle (Figure 5a). The rapid capacity fade within the first 10 cycles signals a continuous yet gradually ceasing SEI growth on carbon during the repeated discharge–charge cycles, as confirmed by a progressive disappearance of the discharge plateau at 0.9−0.8 V (which denotes the SEI formation) upon cycling (Figure 5b). To our best knowledge, such excellent electrochemical performance has rarely been reported for HCs (especially those derived from PFR[30]). Moreover, the volume capacity density of the mPFR-HCA is almost twice that of conventional carbon anode materials, including mesocarbon microbeads (MCMBs, see Figure 5a). In contrast, PFR-HCA shows a much lower initial discharge capacity of 1720 mA·h g^{-1} (805 mA·h cm^{-3}) at 0.1 A g^{-1}, and only 783 mA·h g^{-1} (366 mA·h cm^{-3}) is recovered in the reverse charge process (Figure S13a). Therefore, the ICE of the PFR-HCA (45.5%) is much lower than that of the mPFR-HCA. Since the specific surface area of the mPFR-HCA is significantly larger than that of the PFR-HCA (which means the mPFR-HCA should have a larger initial irreversible capacity contributed by SEI formation than the PFR-HCA), the increased ICE is largely attributable to the ordered structure of the modified carbon, which improves the reversibility of the Li deintercalation reaction upon charging. After the first cycle, the capacity of the PFR-HCA fades rapidly with further cycling. After only 45 cycles, the capacity drops to <200 mA·h g^{-1} (93 mA·h cm^{-3}), and it continues to get lower until only ~110 mA·h g^{-1} (51 mA·h cm^{-3}) is preserved after 100 cycles.

With a much enhanced kinetics upon Li storage, the mPFR-HCA also shows impressive high-rate performances, stably delivering almost 4 times than capacities of PFR-HCA at the same current densities (Figure 5e,f and Figure S12b). After the current density is directly reduced from 5 to 0.1 A g^{-1}, the capacity of mPFR-HCA quickly recovers to 1190 mA·h g^{-1} (826 mA·h cm^{-3}), while the PFR-HCA can be restored to merely ~250 mA·h g^{-1} (117 mA·h cm^{-3}) (Figure 5e and Figure S12b). An extended cycling test at 1 A g^{-1} has shown that the mPFR-HCA preserves an initial charge capacity of 822 mA·h g^{-1} (570 mA·h cm^{-3}) and retains a reversible capacity of 401 mA·h g^{-1} (278 mA·h cm^{-3}) after 1000 cycles, which means an average capacity loss of 0.42 mA·h g^{-1} (0.29 mA·h cm^{-3}) per cycle (Figure 5i). In comparison, the reversible capacity (~30 mA·h g^{-1} or 14 mA·h cm^{-3}) delivered by the PFR-HCA at the same current density is almost negligible (Figure S13c).

Electrochemical Properties of Na-Ion Battery. Graphitized structures have been reported to be unsuitable for Na storage due to a mismatch of the ionic size of Na$^+$ with the spacing of the carbon interlayer. Herein, with an expanded carbon interlayer spacing of ~0.4 nm and carbon micropores of ~0.8 nm, Na storage has been proved feasible in mPFR-HCA.[21] According to the CVs, the mPFR-HCA shows a broad peak starting from 1.0 V in the initial cathodic process (Figure S11b), denoting continuous Na storage in the first carbon micropores and then orderly packed carbon interlayers. The reverse anodic process is accompanied by two even broader oxidation peaks (Figure S11b), denoting Na de-intercalations from different carbon structures of the mPFR-HCA. From the second scan, the CVs become highly consistent (Figure S11b), which means the reaction between mPFR-HCA and Na has reached its electrochemically stable state. Due to the disordered structure of PFR-HCA, the Na intercalation peak during the

initial cathodic CV scan weakens significantly (Figure S11d). On the other hand, there is nearly no obvious oxidation peak in the reverse anodic process (Figure S11d), indicating a sluggish kinetics and a poor reversibility of PFR-HCA upon Na de-intercalation. In the subsequent scans, the reduction peaks continue to decay, which further supports the electrochemical instability of PFR-HCA.

The electrochemical performance of mPFR-HCA in prototype Na half-cells is also impressive. Cycled at 0.1 A g^{-1}, the above carbon electrode can output high capacities of 745 mA·h g^{-1} (517 mA·h cm^{-3}) and 245 mA·h g^{-1} (170 mA·h cm^{-3}) separately upon initial discharge and charge, while maintaining highly consistent GDC profiles in the subsequent cycles (Figure 5c,d). After 100 cycles, a reversible capacity of 155 mA·h g^{-1} (108 mA·h cm^{-3}) is still maintained (Figure 5c,d). In comparison, the PFR-HCA can output an initial discharge capacity of merely 530 mA·h g^{-1} and suffers a quick capacity fade from the initial charge, yielding a much lower capacity of 90 mA·h g^{-1} after 100 cycles (Figure S13d). In testing of the rate performance of these carbons, the mPFR-HCA showed stable GDC profiles upon a gradual increase in the current density from 0.1 to 5 A g^{-1} (Figure 5h), preserving a reversible capacity of 55 mA·h g^{-1} (38 mA·h cm^{-3}) at an extremely high current density of 5 A g^{-1} (when the PFR-HCA showed almost no capacity; see Figure 5g and Figure S12e). In the extended cycling test at 1 A g^{-1}, the carbon can deliver a reversible capacity of 113 mA·h g^{-1} (78 mA·h cm^{-3}) after 1000 steady cycles (Figure 5j), which is 3−4 times the capacity delivered by the PFR-HCA (~40 mA·h g^{-1} or 19 mA·h cm^{-3}, see Figure S13f).

Mechanism for Energy Storage. The electrochemical advantages of the mPFR-HCA in rechargeable Li/Na batteries can be ascribed to its predominant structural advantages. On one hand, the expanded nanographites and carbon micropores provide more intercalation and interfacial storage sites for Li$^+$/Na$^+$, while the increased content of sp^2 carbon leads to a higher hydrogen content, which is beneficial for storage via the exchange route.[59] Hence, a much higher storage capability is observed on the mPFR-HCA. In view of the high oxygen contents in both carbons (Table S1), their effect on the energy storage of HC cannot be neglected. A residual excessive oxygen would inevitably lead to poorer performance since it reduces the electric conductivity of carbon. However, the catalysis by Fe consumes a certain amount of internal oxygen by generating Fe$_2$O$_3$ (as demonstrated by Figure S4a), which results in a lowered O content in the mPFR-HCA and, thereby, better electronic conduction. The etching by nitric acid introduces some oxygen on the surface of the carbons (Table S1 and Figure 3c). With an ordered nanostructure of carbon to facilitate cation migration (Figure 6), these oxygen groups in the mPFR-HCA react irreversibly with the Li/Na during the initial discharge process (as demonstrated by the CV profiles in Figure S11a,b), which depletes the excessive oxygen and contributes to an improved Coulombic efficiency from the second cycle. On the other hand, the porous, interconnected carbon network stabilizes the electrochemical interface between the carbon and the electrolyte (as proved by stable SEI formation on the fiber surface of the mPFR-HCA upon repeated discharge and charge in Figure S14). All these add up to fast and stable Li/Na storage and account for the excellent cycling stability and favorable rate performance of the mPFR-HCA (Figure 6).
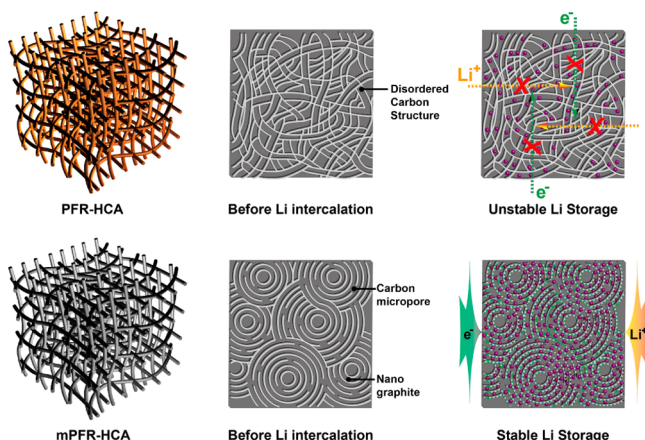
Figure 6. Proposed Li storage mechanism for the ordered expanded nanographite domain of mPFR-HCA and the turbostratic microarchitecture of PFR-HCA.

Also, it is noted that mPFR-HCA shows a lower ICE and capacity in the Na half-cell than in the Li half-cell. This phenomenon directly relates to the pore structure of the carbon. Although the chemical modification yields expanded nanographite domains, there are still graphite layers not fully expanded (Figure 2c), which are apparently unfavorable for Na storage. Therefore, Na^+ ions are preferably stored in some fully expanded graphite layers and the micropores of the mPFR-HCA (while Li^+ can be stored in all the graphite layers and the C micropores), as is demonstrated by the sloped GDC profiles of the mPFR-HCA anode in Na half-cells (Figure 5d). Hence, the mPFR-HCA anode shows a lower Na storage capacity. Further, with the lower initial Na intercalation capacity, the irreversible discharge capacity due to SEI formation will contribute more to the total initial discharge capacity of the mPFR-HCA anode in Na half-cells, resulting in a lower ICE.

Even though other transition metals (such as Co and Ni) have similar catalytic graphitization effects to HCs, Co/Ni-catalyzed PFR-based carbons (labeled as PFR-HCA-Co and PFR-HCA-Ni) show only slightly higher capacities in rechargeable Li batteries compared with the unmodified one (Figure S15), yet the performance is far inferior to that of the mPFR-HCA. We believe a stronger chelation of phenol with Fe^{3+} than with Co^{2+} and Ni^{2+} is responsible for such an improvement, which leads to a more homogeneous dispersion of Fe^{3+} in the chain segments of polymers, so that a more efficient catalytic graphitization and microstructure evolution occur during the modification process.

CONCLUSION

In summary, the chelation of metal ions with precursors is beneficial to improve the dispersion of metal catalysts in carbon precursors, which gives a more efficient catalytic graphitization than the conventional methods. At high temperatures, Fe breaks the sp^3 carbon bridges between graphene sheets, leaving the graphene sheets free to rearrange. The chemical modification by Fe^{3+} generates expanded nanographite and C micropores. Based on this concept, we have successfully developed a facile chemical modification strategy to fabricate hard carbon anodes with stable chemistry and fast kinetics for use in rechargeable Li/Na batteries. The key enabling such a strategy lies in the embedding of highly conductive and ordered nanocarbon structures into a three-dimensionally interconnected carbon network, which ensures efficient ion diffusion and fast electron migration and provides sufficient storage sites to trigger a high-capacity and stable electrochemistry upon energy storage. The structural merits of the modified carbon lead to excellent Li/Na storage performance, which gives gravimetric specific capacities and volumetric capacity densities far beyond those of the other HCs reported and the conventional carbon anodes such as MCMB (Tables S2 and S3), long life spans to last 1000 cycles with high capacity retentions, and superior rate capabilities. The preparation method in this work is facile and easily scaled up; moreover, considering the significant cost advantage of the PFR-derived HCs, our carbon anode is expected to promise practical, high-energy batteries.

ASSOCIATED CONTENT

Ⓢ Supporting Information

The Supporting Information is available free of charge on the ACS Publications website at DOI: 10.1021/jacs.6b06673.

> Detailed methods for the preparation of mPFR-HCA, PFR-HCA, PFR-HCA-Co, and PFR-HCA-Ni; structural and electrochemical characterization of these carbons; chemical diffusion coefficients; and theoretical calculation results, including Figures S1−S15 and Tables S1−S3 (PDF)

AUTHOR INFORMATION

Corresponding Authors

*shyu@ustc.edu.cn
*jgoodenough@mail.utexas.edu

Author Contributions

#Z.-L.Y. and S.X. contributed equally to this work.

Notes

The authors declare no competing financial interest.

REFERENCES

(1) Melot, B. C.; Tarascon, J. M. *Acc. Chem. Res.* **2013**, *46*, 1226.
(2) Kim, S.-O.; Manthiram, A. *ACS Appl. Mater. Interfaces* **2015**, *7*, 14801.
(3) Ha, K.-H.; Woo, S. H.; Mok, D.; Choi, N.-S.; Park, Y.; Oh, S. M.; Kim, Y.; Kim, J.; Lee, J.; Nazar, L. F.; Lee, K. T. *Adv. Energy Mater.* **2013**, *3*, 770.
(4) Jian, Z.; Xing, Z.; Bommier, C.; Li, Z.; Ji, X. *Adv. Energy Mater.* **2016**, *6*, 1501874.

(5) Tahir, M. N.; Oschmann, B.; Buchholz, D.; Dou, X.; Lieberwirth, I.; Panthöfer, M.; Tremel, W.; Zentel, R.; Passerini, S. *Adv. Energy Mater.* **2016**, *6*, 1501489.

(6) Cheng, F.; Liang, J.; Tao, Z.; Chen, J. *Adv. Mater.* **2011**, *23*, 1695.

(7) Jiang, J.; Li, Y.; Liu, J.; Huang, X.; Yuan, C.; Lou, X. W. *Adv. Mater.* **2012**, *24*, 5166.

(8) Qian, J.; Wu, X.; Cao, Y.; Ai, X.; Yang, H. *Angew. Chem.* **2013**, *125*, 4731.

(9) Yu, H.; Ren, Y.; Xiao, D.; Guo, S.; Zhu, Y.; Qian, Y.; Gu, L.; Zhou, H. *Angew. Chem., Int. Ed.* **2014**, *53*, 8963.

(10) Yue, Y.; Binder, A. J.; Guo, B.; Zhang, Z.; Qiao, Z.-A.; Tian, C.; Dai, S. *Angew. Chem., Int. Ed.* **2014**, *53*, 3134.

(11) Wang, H.-G.; Wu, Z.; Meng, F.-L.; Ma, D.-L.; Huang, X.-L.; Wang, L.-M.; Zhang, X.-B. *ChemSusChem* **2013**, *6*, 56.

(12) Liu, J.; Kopold, P.; Wu, C.; van Aken, P. A.; Maier, J.; Yu, Y. *Energy Environ. Sci.* **2015**, *8*, 3531.

(13) Su, D. W.; Dou, S. X.; Wang, G. X. *J. Mater. Chem. A* **2014**, *2*, 11185.

(14) Goodenough, J. B.; Park, K.-S. *J. Am. Chem. Soc.* **2013**, *135*, 1167.

(15) Park, Y.-U.; Seo, D.-H.; Kwon, H.-S.; Kim, B.; Kim, J.; Kim, H.; Kim, I.; Yoo, H.-I.; Kang, K. *J. Am. Chem. Soc.* **2013**, *135*, 13870.

(16) Peng, L.; Peng, X.; Liu, B.; Wu, C.; Xie, Y.; Yu, G. *Nano Lett.* **2013**, *13*, 2151.

(17) Yao, Y.; McDowell, M. T.; Ryu, I.; Wu, H.; Liu, N.; Hu, L.; Nix, W. D.; Cui, Y. *Nano Lett.* **2011**, *11*, 2949.

(18) Zhu, H.; Jia, Z.; Chen, Y.; Weadock, N.; Wan, J.; Vaaland, O.; Han, X.; Li, T.; Hu, L. *Nano Lett.* **2013**, *13*, 3093.

(19) Pasta, M.; Wessells, C. D.; Huggins, R. A.; Cui, Y. *Nat. Commun.* **2012**, *3*, 1149.

(20) Sun, Y.; Zhao, L.; Pan, H.; Lu, X.; Gu, L.; Hu, Y.-S.; Li, H.; Armand, M.; Ikuhara, Y.; Chen, L.; Huang, X. *Nat. Commun.* **2013**, *4*, 1870.

(21) Wen, Y.; He, K.; Zhu, Y.; Han, F.; Xu, Y.; Matsuda, I.; Ishii, Y.; Cumings, J.; Wang, C. *Nat. Commun.* **2014**, *5*, 4033.

(22) Yang, Z.; Zhang, J.; Kintner-Meyer, M. C.; Lu, X.; Choi, D.; Lemmon, J. P.; Liu, J. *Chem. Rev.* **2011**, *111*, 3577.

(23) Gogotsi, Y.; Simon, P. *Science* **2011**, *334*, 917.

(24) Xin, S.; Guo, Y.-G.; Wan, L.-J. *Acc. Chem. Res.* **2012**, *45*, 1759.

(25) Ma, L.; Hendrickson, K. E.; Wei, S.; Archer, L. A. *Nano Today* **2015**, *10*, 315.

(26) Chen, C.; Wen, Y.; Hu, X.; Ji, X.; Yan, M.; Mai, L.; Hu, P.; Shan, B.; Huang, Y. *Nat. Commun.* **2015**, *6*, 6929.

(27) Liu, C.; Li, F.; Ma, L. P.; Cheng, H. M. *Adv. Mater.* **2010**, *22*, E28.

(28) Wang, H.; Dai, H. *Chem. Soc. Rev.* **2013**, *42*, 3088.

(29) Li, H.; Wang, Z.; Chen, L.; Huang, X. *Adv. Mater.* **2009**, *21*, 4593.

(30) Fang, Y.; Lv, Y.; Che, R.; Wu, H.; Zhang, X.; Gu, D.; Zheng, G.; Zhao, D. *J. Am. Chem. Soc.* **2013**, *135*, 1524.

(31) Liu, J.; Yang, T.; Wang, D. W.; Lu, G. Q.; Zhao, D.; Qiao, S. Z. *Nat. Commun.* **2013**, *4*, 2798.

(32) Odkhuu, D.; Jung, D. H.; Lee, H.; Han, S. S.; Choi, S.-H.; Ruoff, R. S.; Park, N. *Carbon* **2014**, *66*, 39.

(33) Stevens, D. A.; Dahn, J. R. *J. Electrochem. Soc.* **2000**, *147*, 1271.

(34) Dahn, J. R.; Zheng, T.; Liu, Y. H.; Xue, J. S. *Science* **1995**, *270*, 590.

(35) Xu, Y.; Lin, Z.; Zhong, X.; Papandrea, B.; Huang, Y.; Duan, X. *Angew. Chem., Int. Ed.* **2015**, *54*, 5345.

(36) Tian, L.; Zhuang, Q.; Li, J.; Wu, C.; Shi, Y.; Sun, S. *Electrochim. Acta* **2012**, *65*, 153.

(37) He, Y.-S.; Bai, D.-W.; Yang, X.; Chen, J.; Liao, X.-Z.; Ma, Z.-F. *Electrochem. Commun.* **2010**, *12*, 570.

(38) Chen, R.; Zhao, T.; Lu, J.; Wu, F.; Li, L.; Chen, J.; Tan, G.; Ye, Y.; Amine, K. *Nano Lett.* **2013**, *13*, 4642.

(39) Zhou, H.; Zhu, S.; Hibino, M.; Honma, I.; Ichihara, M. *Adv. Mater.* **2003**, *15*, 2107.

(40) Huang, X.; Yu, H.; Chen, J.; Lu, Z.; Yazami, R.; Hng, H. H. *Adv. Mater.* **2014**, *26*, 1296.

(41) Yang, X.; Zhang, L.; Zhang, F.; Huang, Y.; Chen, Y. *ACS Nano* **2014**, *8*, 5208.

(42) Chen, Y.; Li, X.; Park, K.; Song, J.; Hong, J.; Zhou, L.; Mai, Y.-W.; Huang, H.; Goodenough, J. B. *J. Am. Chem. Soc.* **2013**, *135*, 16280.

(43) Yu, Z.-L.; Wu, Z.-Y.; Xin, S.; Qiao, C.; Yu, Z.-Y.; Cong, H.-P.; Yu, S.-H. *Chem. Mater.* **2014**, *26*, 6915.

(44) Zhao, M.; Song, H.; Chen, X.; Lian, W. *Acta Mater.* **2007**, *55*, 6144.

(45) Oya, A.; Otani, S. *Carbon* **1979**, *17*, 131.

(46) Oya, A.; Marsh, H. *J. Mater. Sci.* **1982**, *17*, 309.

(47) Zhao, M.; Song, H. *J. Mater. Sci. Technol.* **2011**, *27*, 266.

(48) Lee, S. W.; Yabuuchi, N.; Gallant, B. M.; Chen, S.; Kim, B. S.; Hammond, P. T.; Shao-Horn, Y. *Nat. Nanotechnol.* **2010**, *5*, 531.

(49) Paraknowitsch, J. P.; Zhang, J.; Su, D.; Thomas, A.; Antonietti, M. *Adv. Mater.* **2010**, *22*, 87.

(50) Jackson, S. T.; Nuzzo, R. G. *Appl. Surf. Sci.* **1995**, *90*, 195.

(51) Xu, F.; Tang, Z.; Huang, S.; Chen, L.; Liang, Y.; Mai, W.; Zhong, H.; Fu, R.; Wu, D. *Nat. Commun.* **2015**, *6*, 7221.

(52) Hontoria-Lucas, C.; Lopez-Peinado, A. J.; Lopez-Gonzalez, J. D.; Rojas-Cervantes, M. L.; Martin-Aranda, R. M. *Carbon* **1995**, *33*, 1585.

(53) He, H.; Klinowski, J.; Forster, M.; Lerf, A. *Chem. Phys. Lett.* **1998**, *287*, 53.

(54) Freitas, J. C. C.; Bonagamba, T. J.; Emmerich, F. G. *Carbon* **2001**, *39*, 535.

(55) Maniwa, Y.; Sato, M.; Kume, K.; Kozlov, M. E.; Tokumoto, M. *Carbon* **1996**, *34*, 1287.

(56) Ai, K.; Liu, Y.; Ruan, C.; Lu, L.; Lu, G. *Adv. Mater.* **2013**, *25*, 998.

(57) Zheng, T.; Liu, Y.; Fuller, E. W.; Tseng, S.; von Sacken, U.; Dahn, J. R. *J. Electrochem. Soc.* **1995**, *142*, 2581.

(58) Zhou, X.; Dai, Z.; Liu, S.; Bao, J.; Guo, Y.-G. *Adv. Mater.* **2014**, *26*, 3943.

(59) Zhou, P.; Papanek, P.; Bindra, C.; Lee, R.; Fischer, J. E. *J. Power Sources* **1997**, *68*, 296.